

Ion acceleration processes at reforming collisionless shocks

R. E. Lee* and S. C. Chapman†

*Space and Astrophysics Group, Physics Department,
University of Warwick, Coventry, CV4 7AL, UK*

R. O. Dendy‡

UKAEA Culham Division, Culham Science Centre, Abingdon, Oxfordshire, OX14 3DB, UK

(Dated: June 28, 2018 11:02)

The identification of pre-acceleration mechanisms for cosmic ray ions in supernova remnant shocks is an important problem in astrophysics. Recent particle-in-cell (PIC) shock simulations have shown that inclusion of the full electron kinetics yields non-time-stationary solutions, in contrast to previous hybrid (kinetic ions, fluid electrons) simulations. Here, by running a PIC code at high phase space resolution, ion acceleration mechanisms associated with the time dependence of a supercritical collisionless perpendicular shock are examined. In particular the components of $\int \mathbf{F} \cdot \mathbf{v} dt$ are analysed along trajectories for ions that reach both high and low energies. Selection mechanisms for the ions that reach high energies are also examined. In contrast to quasi-stationary shock solutions, the suprathermal protons are selected from the background population on the basis of the time at which they arrive at the shock, and thus are generated in bursts.

PACS numbers: 98.38.Mz 52.65.Rr 98.70.Sa

I. INTRODUCTION

Understanding the initial acceleration mechanisms for Galactic cosmic rays remains an outstanding problem in astrophysics. From energy balance considerations, supernova remnants (SNRs) provide the most likely kinetic energy source to sustain the cosmic ray population. The local acceleration of electrons has been indirectly observed at the expanding shock front of SNRs (see, for example, Ref. [1]). However protons form the majority constituent of Galactic cosmic rays, and until recently observational evidence to link SNRs to local ion acceleration has been lacking. X-ray and γ -ray data from supernova remnant RX J1713.7-3946 [2] show energy spectra that can only be explained by accelerated ions. Several mechanisms are postulated to accelerate particles at SNR shocks. Fermi acceleration [3], which arises as a particle repeatedly scatters off turbulent structures on either side of the shock, is in principle capable of accelerating ions to high energies [4]. However, to work effectively an initial suprathermal population is required so that particles can re-cross the shock front [5]. The identification and analysis of pre-acceleration mechanisms that can select and initiate the energisation of completely non-relativistic ions at SNR shocks from the background plasma is the subject of this paper.

The Rankine-Hugoniot relations [6] can be used to determine the discontinuity in bulk plasma parameters across a collisionless shock; that is, a shock where the

particle mean free path is much greater than length scales of interest. These relations are derived by applying the magnetohydrodynamic (MHD) conservation equations in the far upstream and downstream limits, away from the shock. Further conditions are imposed by the fact that a shock must also increase entropy, so that no subsonic flow can spontaneously become supersonic. For an Alfvénic Mach number $M_A \gtrsim 3$, the shock is supercritical in that the increase in entropy, and in ion heating, required by the Rankine-Hugoniot relations is achieved via the ion kinetics; at least in part, by reflection of a fraction of upstream ions at the shock. The generic supercritical, quasi-perpendicular, collisionless shock in which ions reflect and gyrate in a foot region upstream has been suggested by hybrid (particle ions, fluid electrons) simulations (see, for example, Refs. [7, 8, 9]), and confirmed by in-situ observations of the Earth's bow shock [10].

To study the acceleration of ions and electrons, a fully kinetic treatment is in principle necessary for both species, and this can be closely approximated by particle-in-cell (PIC) techniques. Physical mechanisms operating on electron kinetic lengthscales and timescales are significant both for aspects of macroscopic structure (for example, the shock ramp width scales as c/ω_{pe}), and for microscopic processes affecting the ions (such as caviton formation and dissolution). Whether such effects are important in any given scenario can be estimated, to some extent, by analytical means, as we discuss in detail below. Importantly, however, it is known that inclusion of the full electron kinetics can significantly alter the dynamics of the shock. For example, hybrid simulations for certain parameters [8, 9] produce time-stationary shock solutions, whereas for the same parameters PIC simulations reveal a dynamic, reforming, shock structure. Furthermore the extent to which an individual ion responds to phenomena on electron kinetic scales must depend on

*leer@astro.warwick.ac.uk

†Also at Radcliffe Institute for Advanced Study, Harvard University, USA

‡Also at Space and Astrophysics Group, Physics Department, University of Warwick, Coventry, CV4 7AL, UK

that ion's cyclotron radius, and hence its energy. It follows that for studies of ion acceleration at shocks, as in the present paper, retention of full electron kinetics is desirable in order to resolve fully the shock dynamics (see also Refs. [11, 12]) and the ion dynamics. We have previously presented results of PIC code simulations [12, 13, 14] that have high resolution in real space and phase space, over relatively long run times, for parameters relevant to shocks at supernova remnants. Our most recent results [12] show that the time-dependent electromagnetic fields at the reforming shock can accelerate inflow ions from background to suprathermal energies. This provides a source population which may subsequently be accelerated to produce high energy cosmic rays.

In the present paper, we focus on the specific nature of this ion acceleration mechanism. This requires careful examination of the physics of the interaction between particles and fields as they evolve over time. We first introduce a methodology for simplifying the raw data, obtained on spatio-temporal scales spanning those of the electrons and ions, into data suitable for examining events on the spatio-temporal scales of interest for ion acceleration. We then examine the detailed dynamics of the ion interactions with the shock front, including a comparison between ions that eventually reach the highest and lowest energies downstream. The time at which particles are incident on the temporally evolving shock structure is found to be a key discriminant in the subsequent energisation.

II. SIMULATION METHOD

The technical basis of the simulations was recently reported in Ref. [12]; let us reiterate briefly for completeness. We use a relativistic electromagnetic particle-in-cell (PIC) code to simulate the structure and evolution of a supercritical, collisionless, perpendicular magnetosonic shock. In a PIC simulation the distribution functions of all particle species are represented by computational super-particles, whilst the electromagnetic fields are defined on a spatial grid. Particle trajectories are evolved from the fields via the Lorentz force, then the fields are evolved from the new particle positions via Maxwell's equations [15]. The code we use to simulate the shock is based on that described in Ref. [16], and has been used recently to examine electron and ion acceleration in SNR shocks [12, 13, 14, 17]. All vector fields, bulk plasma properties and particle velocities are functions of one spatial co-ordinate (x), and time. This simplification enables detailed phase space resolution for relatively long run times, however it constrains magnetic fields: since $\nabla \cdot \mathbf{B} = 0$ we have $B_x = \text{constant}$, taken as zero here in strict perpendicular geometry. PIC simulations in two spatial dimensions (see, for example, Ref. [18]) that relax this constraint yield overall shock dynamics that are consistent with the results seen here.

We present results from simulations of a perpendicular shock propagating into a magnetic field ($B_{z,1}$) of 1×10^{-7} Tesla, a value consistent with those expected at supernova remnants [19]. The ratio of electron plasma frequency to electron cyclotron frequency $\omega_{pe}/\omega_{ce} = 20$, and the upstream ratio of plasma thermal pressure to magnetic field pressure, $\beta = 0.15$. The shock has an Alfvénic Mach number (M_A) of 10.5, and the simulation mass ratio for ions and electrons $M_R = m_i/m_e = 20$, in common with Refs. [12, 13, 14, 20]. This reduced mass ratio is necessary to enable ion and electron time scales to be captured within the same simulation, with reasonable computational overheads. Previous PIC simulations for physical, and a range of non-physical, m_i/m_e show a variety of kinetic instabilities in the foot region [11, 21]. Here we find that the ion dynamics are insensitive to structures on electron scales, associated with these instabilities.

We also follow Refs. [12, 13, 14, 20] in using the piston method (see, for example, Ref. [9], and references therein) to set up the shock. Particles are injected on the left hand side of the simulation box with a drift speed v_{inj} , modified by a small random velocity drawn from a thermal distribution, characterised by u_{therm} . At the particle injection boundary, the magnetic field ($B_{z,1}$) is constant and the electric field ($E_{y,1}$) is calculated self-consistently. The right hand boundary is taken to be a perfectly conducting, perfectly reflecting wall. Particles reflect off this boundary, and a shock then forms, propagating to the left through the simulation box; sufficient time is allowed for the shock to propagate sufficiently far upstream that the boundary conditions are no longer important. The size of a grid cell is defined as a Debye length (λ_D), and the time step is set to less than λ_D/c , for numerical stability reasons [22]. To enable the shock and particle dynamics to be followed over extended time-scales, whilst retaining high particle density, a simple shock following algorithm is implemented. This holds the peak in magnetic field at $8\lambda_{ci}$ from the left-hand boundary (for details see Ref. [14], Appendix A). This distance is chosen so that no particles that are reflected off the shock subsequently reach the upstream boundary, whilst it leaves a significant region of the simulation box (around $20\lambda_{ci}$) downstream.

III. RESULTS

Full simulation of the non-time-stationary features of a collisionless shock requires the retention of electron dynamics; see, for example Ref. [8]. However, resolving features on electron scales also introduces processes that do not couple strongly to the processes that operate on ion scales, which are the focus of the present paper. For example, the observed electron scale electrostatic solitary wave structures can lead to electron acceleration [14], but do not significantly affect the ions. As an aid to interpreting the interactions occurring within a PIC simulation that give rise to ion acceleration, we present

a framework which distinguishes structure and dynamics on electron kinetic scales from those relevant to ions. The ion trajectories that we present here are however all evolved self-consistently within the full electro-magnetic fields of the PIC simulation

A. Electric Potential on Ion Spatio-Temporal Scales

Resolving the full electron and ion kinetics in the PIC simulation establishes two distinct spatio-temporal scales on which physical processes can occur. On sufficiently fast time scales and short length scales there are, for example, plasma oscillations that lead to fluctuations in charge density. However, on longer spatio-temporal scales the plasma is quasi-neutral but still supports bulk electric fields. We can obtain an expression for these bulk fields by treating the plasma as two fluids, ions and electrons (for a more general multi-fluid treatment see, for example Refs. [23, 24, 25]), governed by the momentum equations

$$n_e m_e \frac{D\mathbf{v}_e}{Dt} = -en_e(\mathbf{E} + \mathbf{v}_e \wedge \mathbf{B}) - \nabla P_e - n_e \nu_{ei} \mathbf{v}_e, \quad (1)$$

$$n_i m_i \frac{D\mathbf{v}_i}{Dt} = q_i n_i (\mathbf{E} + \mathbf{v}_i \wedge \mathbf{B}) - \nabla P_i - n_i \nu_{ie} \mathbf{v}_i. \quad (2)$$

The final terms in Eqs. (1) and (2) represent momentum transfer between species via forces not included in the macroscopic fields. Here, we can assume that on the time-scale of ion interaction with the shock, these terms are negligible for the ions.

We wish to consider space and time varying electro-magnetic fields that only affect the ions, so that on ion scales we can take the limit in which the electrons respond instantaneously as a charge neutralising fluid. This implies a vanishing electron inertial term, the “massless electron fluid” limit often used in hybrid codes:

$$m_e \frac{D\mathbf{v}_e}{Dt} \rightarrow 0. \quad (3)$$

We neglect the electron pressure gradient because it is significant on electron, rather than ion scales, however we anticipate that this approximation will be least reliable in the shock ramp.

We can relate \mathbf{v}_e directly to \mathbf{v}_i via the current. On the spatio-temporal scales on which the electron-proton ($q_i = e$) plasma is quasi-neutral ($n_i \simeq n_e = n$),

$$\mathbf{J} \simeq en(\mathbf{v}_i - \mathbf{v}_e). \quad (4)$$

Substitution for \mathbf{v}_e from Eq. (4) into Eq. (1) then gives

$$0 \simeq \mathbf{E} + \left[\mathbf{v}_i - \frac{\mathbf{J}}{en} \right] \wedge \mathbf{B}. \quad (5)$$

Consistent with this low frequency approximation we neglect the displacement current (the non-radiative limit),

giving Ampère’s law

$$\nabla \wedge \mathbf{B} = \mu_0 \mathbf{J}. \quad (6)$$

This implies the standard expression

$$\mathbf{J} \wedge \mathbf{B} = -\frac{1}{\mu_0} \left[\frac{\nabla B^2}{2} - (\mathbf{B} \cdot \nabla) \mathbf{B} \right]. \quad (7)$$

Together, Eqs. (5) and (7) give

$$0 \simeq \mathbf{E} + \mathbf{v}_i \wedge \mathbf{B} + \frac{1}{\mu_0 en} \left[\frac{\nabla B^2}{2} - (\mathbf{B} \cdot \nabla) \mathbf{B} \right], \quad (8)$$

which can then be rearranged to yield \mathbf{E} .

In the one dimensional geometry of our simulation Eq. (8) can be simplified by noting $\nabla \equiv (\partial_x, 0, 0)$, thus $(\mathbf{B} \cdot \nabla) \mathbf{B} = 0$. Further simplification arises if we note that generally in our simulations, $v_z \ll v_y$, thus $(v_{i,y} B_z - v_{i,z} B_y) \simeq v_{i,y} B_z$. Rearranging a simplified Eq. (8) then gives

$$E_{x,i} \simeq -\frac{1}{en\mu_0} \frac{\partial(B_z^2/2 + B_y^2/2)}{\partial x} - v_{i,y} B_z, \quad (9)$$

$$E_{y,i} \simeq v_{i,x} B_z. \quad (10)$$

Here $E_{x,i}$ is the x component, and $E_{y,i}$ the y component, of the electric field on the slow, ion spatio-temporal scales on which the plasma is quasi-neutral.

Substitution of our simplified, ion scale, electric field from Eq. (8), into the ion force equation Eq. (2), leads to an expression whose x component is

$$nm_i \frac{D\mathbf{v}_i}{Dt} \Big|_x \simeq -\frac{1}{\mu_0} \frac{\partial(B_z^2/2 + B_y^2/2)}{\partial x} - \frac{\partial P_i}{\partial x}. \quad (11)$$

It follows from Eq. (11) that the bulk force on the ion fluid is due to gradients in magnetic and plasma pressure. The potentials (which act on individual particles) follow from Eqs. (9) and (10).

Figure 1 demonstrates the extent to which this approximate analytical treatment provides a guide to the ion behaviour that is calculated from first principles in the PIC code. It compares the time evolution of the potential, $\phi = \int E_x dx$, obtained directly from the PIC code, to that calculated on ion scales, $\phi_i = \int E_{x,i} dx$, using Eq. (9). The path chosen for the spatial integration is that of an ion that reaches a high energy on leaving the shock front. Fig. 1 demonstrates that $E_{x,i}$ defined in Eq. (9) is a useful guide, and hence the analysis above captures much of the key physics. The ion scale bulk potential essentially averages over the small scale fluctuations of the “raw” potential. We can see from Fig. 1, however, that the average values of ϕ_i depart from that of the full potential ϕ where the ion interacts with the shock ramp: first during a reflection at $t = 3.5 - 3.7$, and during a subsequent transmission to downstream at $t = 5 - 5.2 \times 2\pi\omega_{ci}^{-1}$. In the discussion below, we will calculate the ion energetics from the full electromagnetic fields of the PIC simulation.

B. Ion Acceleration

To study the physical processes that cause ion acceleration, we evaluate the changes in kinetic energy of ions during their interaction with the shock. Here the ion Lorentz factor $\gamma \sim 1$, therefore we can neglect relativistic effects. We have

$$\mathbf{F} = m \frac{d\mathbf{v}}{dt} = q(\mathbf{E} + \mathbf{v} \wedge \mathbf{B}) \quad (12)$$

where, in our collisionless plasma, \mathbf{E} and \mathbf{B} in the Lorentz force refer to the fields in the PIC simulation. Thus

$$\mathbf{F} \cdot \mathbf{v} = \frac{d}{dt} \left(\frac{1}{2} m v^2 \right) = q \mathbf{E} \cdot \mathbf{v} \quad (13)$$

Integration along a computed ion trajectory then implies that the kinetic energy acquired is:

$$\frac{1}{2} m v^2 = q \int_{\text{trajectory}} \mathbf{E} \cdot \mathbf{v} dt. \quad (14)$$

1. Highly energetic ions

Previous PIC simulations [12] have shown that the downstream proton population has a continuous distribution of energies from zero up to ~ 6 times the ion injection energy, $\mathcal{E}_{inj} = \frac{1}{2} m v_{inj}^2$, in the frame in which the downstream plasma is at rest. We now examine the dynamics of these ions in more detail. Figure 2 presents the results of evaluating Eq. (14) for a selected group of protons that become highly energised. The top panel (panel 1) displays the kinetic energy over time, calculated from $\int q \mathbf{E} \cdot \mathbf{v} dt$ along the particle trajectory. Panel 2 shows only the x -component, $\int q E_x v_x dt$ normal to the shock, and panel 3 shows only the y -component along the shock front. The z -component is omitted as it remains identically zero, due to the configuration of the simulation domain. Panel 4 displays the potential, $\phi = \int E_x dx$, computed directly from the PIC code, at the x -position of the ions at the current time. Panel 5 shows the y -positions. In the lowest panel (panel 6) the x -positions are shown in relation to the spatio-temporally evolving potential structure on ion scales, $\phi_i = \int E_{x,i} dx$ computed using Eq. (9). Comparison of this panel with Fig. 8 of Ref. [12] shows that ϕ_i captures the qualitative features of the electromagnetic fields. To complement this information, Fig. 3 shows the trajectory of a high energy ion in the x - y plane (in the simulations we evolve the three components of the particle velocity $\mathbf{v}(x, t)$, and these can be integrated to provide a trajectory in three dimensional configuration space). As with all results in this paper, data is presented in the downstream rest frame, and has been obtained from a segment of the simulation when the shock is propagating independently of the boundary conditions. Units are normalised to the upstream ion parameters, that is, λ_{ci} the upstream ion cyclotron radius, and ω_{ci} the upstream ion cyclotron frequency.

Figure 2 shows that the ions that become highly energised remain close in phase space throughout their interactions with the shock. After passing through the shock, local fluctuations in the fields lead to some divergence in the y -component of $\int q \mathbf{E} \cdot \mathbf{v} dt$ and the y -position. Panel 6 shows the shock propagating in the negative x -direction over time, while undergoing reformation cycles. The size and depth of the potential well varies over the course of a reformation cycle, on a time scale comparable to the local ion cyclotron period, as discussed in detail by Lee et al. [12].

If we follow the path through the shock region of an individual ion that eventually reaches high energy, a series of events occurs. The ion is initially co-moving with the plasma at the inflow speed. This corresponds to the linear increase in x -position (panel 6), with no translation in the y -direction (panel 5 and Fig. 3), all at the inflow energy (panel 1). It should be noted that in panel 1, the energies are initially zero, because the start of the integration path for $\int q \mathbf{E} \cdot \mathbf{v} dt$ is chosen to be just inside the simulation domain, where the ions are already co-moving with the plasma. This location is upstream of the shock foot, and the potential in this region is therefore constant, with the only variation due to high frequency fluctuations in \mathbf{E} .

After approximately 3.25 ion cyclotron periods, the ion enters the potential well upstream of the shock front, point *a* in Fig. 2. At this time, the shock is most fully formed, the shock jump is close to maximal, so that the $\partial B^2 / \partial x$ term in the potential from Eq. (9) is close to maximal also. The x -component of $\int q \mathbf{E} \cdot \mathbf{v} dt$ shows a decrease in energy as the ion journeys further into the well (panel 2), with a corresponding decrease in kinetic energy (panel 1); this follows from a negative value for E_x . Between points *a* and *b* there is a decrease in x -velocity as the ion gets closer to the shock and the magnetic field increases, which is accompanied by a weak drift in $-y$, see also Fig. 3.

At the time corresponding to point *b*, the kinetic energy reaches a minimum (panel 1), when the ion is near the deepest point in the potential well (panels 4 and 6). The ion has now stopped its progression toward the shock front (Fig. 3), and reflection back into the upstream region has begun (panel 6).

By time *c* the ion has begun to climb back out of the potential well, away from the shock front (panel 4). After *c*, drift in $+y$ begins as the ions move in $-x$ into the foot region, see also Fig. 3. Meanwhile the x -component of $\int q \mathbf{E} \cdot \mathbf{v} dt$ starts to increase rapidly (panel 2), due to the strength of E_x (shown by the gradient of ϕ , panel 4).

By point *d* the particle has moved back to the extreme upstream edge of the potential well. It then remains moving along a contour of $\phi \simeq 0$ (panels 4 and 6) for a time approximately equal to one upstream ion cyclotron period ($2\pi\omega_{ci}^{-1}$). Between *d* and *e* the value of E_x local to the ion is lower, so that the associated energisation rate is also less; however the positive y -component of the gyromotion continues (panel 5 and Fig. 3), and since the

motional E_y is positive, this gives an energy gain in the y -component $\Delta\mathcal{E}_y = \Delta m v_y^2/2$ (panel 3). The gyromotion of the particle eventually leads to a positive x -component of velocity (Fig. 3), so that at point e the particle finally leaves the extreme upstream edge of the well and passes through the potential well for a second time (panels 4 and 6). This marks the end of a prolonged episode of energy gain, which now stops as y -drift ceases (panels 1 and 3), and the particle settles into its stable downstream gyromotion (Fig. 3). The ions cross the saddle in the potential $\phi(x, t)$ (as shown in panel 6), leading to a brief energy loss then gain via the x -component of $\int q\mathbf{E} \cdot \mathbf{v} dt$ (panel 2), before the ion passes thorough the shock front (point f , panels 3 and 6), and gyrates away from the shock into the downstream region. The ion energy now exceeds its initial value by a factor of approximately six.

In summary there are two stages of acceleration as shown in Fig. 3: normal reflection from the temporarily stationary shock front into the foot region, followed by energisation during transverse drift across the shock front.

2. Weakly energised ions

Further insight into the energisation process can be gained by comparing trajectories for ions that become highly energised (Fig. 2), to those for a group of ions that have only low energies ($\lesssim \mathcal{E}_{inj}$) on finally entering the downstream region (Fig. 4), and remain in the core of the downstream particle distribution.

The trajectories for the ions that are not subsequently energised are initially similar to those for the ions that eventually reach the higher energies. The primary difference is the timing of their first encounter with the shock. We have identified two distinct groups of low energy ions, and these are shown in Fig. 4. The first group arrives at the shock front just as the shock is advancing ($t = 3.1 \times 2\pi\omega_{ci}^{-1}$), and the second when the shock is decaying ($t = 4 \times 2\pi\omega_{ci}^{-1}$).

The reforming shock progresses upstream (downwards in panel 6 of Figs. 2 and 4) in a stepwise fashion. The first group of ions (upper trajectories in panel 6 of Fig. 4) encounter the advancing shock when the shock jump is sufficiently large to cause reflection (between points A and B). Their trajectories up to this point are akin to the trajectories up to point b in Fig. 2 for the ions that have become highly energised: they have entered the foot region (point A) and been deflected in the $-y$ direction, whilst losing energy via a decrease in $\int qE_x v_x dt$. However, at this time the shock speed is maximal, so their velocity component in $-x$ is smaller than that of the shock itself, and the shock overtakes them. They then co-move with the shock front for about an upstream ion cyclotron period, before moving downstream.

On the other hand the second group of ions encounter the shock when the potential is decaying (point A'). They then pass through the potential well (point B'),

and reach the shock without reflection, where their v_\perp increases (Fig. 5) along with the bulk \mathbf{B} field downstream.

Regardless of their energisation or of the details of their dynamics, the guiding center velocity of all ions goes to zero once they have propagated sufficiently far downstream of the shock front. This is to be expected, because the far downstream frame defines the rest frame of the plasma, as noted previously (Figs. 3 and 5).

Of further interest is the y -motion of the two groups of low energy ions (panel 5 of Fig. 4). Those that enter the shock before the high energy ions have little movement of their gyrocenters in y , but those that enter after the high energy ions, have a significant $-y$ drift velocity; see also Fig. 5. Both these patterns are in contrast to the high energy ions that have gyrocenters that drift in the $+y$ direction (panel 5 of Fig. 2, and Fig. 3).

Finally we can compare the kinetic energy gain computed directly from the electromagnetic fields of the PIC simulation, with that given by the fields on ion scales estimated from Eqs. (9) and (10). In Fig. 6 we plot the total kinetic energy as a function of time along the trajectory of an ion that is reflected and reaches suprathermal energy. This plot shows a close correspondence between the two curves, suggesting that the fine structure on electron scales does not affect the final energy gain of these ions. However, as we have seen from Fig. 1, there is a discrepancy between the x -component of the electric field at the shock ramp obtained from the simulation directly, and from Eq. (9). It therefore follows from Fig. 6 that the value of the shock ramp does not strongly affect the overall energy gain of these ions. This is consistent with energisation being associated with electromagnetic fields away from the ramp, the role of the ramp potential being simply to reflect the ions. However, details of the energetics of low energy ions that are not reflected, may depend on the value of the shock ramp potential.

C. Role of Shock Reformation

Having examined the trajectories of ions that reach a variety of energies, let us now examine the selection mechanisms that give rise to different histories and energisation. For a time stationary shock, Burgess et al. [9] examined the origins in phase space of ions that eventually reach differing energies. Particles from the extrema of the velocity space distribution upstream of the shock were found to be preferentially reflected further upstream, and so energised to higher energies; whereas ions from the core of the distribution passed through the shock, moving little or no distance upstream. To establish whether the same selection mechanism is at work in our dynamic reforming shock, we have constructed in Fig. 7 a series of plots that may be compared with Fig. 1 of Ref. [9]. Figure 7 shows the ion phase space (v_x and v_y vs. x) for groups of ions at differing initial perpendicular velocities, at a time when the potential well is at its narrowest, and the reformation cycle has just com-

menced, corresponding to $t = 4 \times 2\pi\omega_{ci}^{-1}$ in Fig. 2. In contrast to the results obtained in Ref. [9] for the case of a time stationary shock, we find that at a reforming shock, ions that are initially in the core of the distribution, as well as those from the tails, are reflected back into the foot region. Also, the distance travelled back into the foot region (and hence the energy gained) appears independent of the initial perpendicular velocity of the ions. Whether or not a given ion is reflected depends on its normal velocity in comparison with the time-dependent shock potential. Thus the timing at which ions arrive at the shock front determines their final location in velocity space.

Overall, examination of the shock dynamics in relation to ion trajectories shows that the ions that are ultimately highly energised (Fig. 2) reflect from the shock front just as it becomes stationary, and pass through the foot region saddle in $\phi(x, t)$ (panel 6). The ions that meet the shock front prior to this (upper group in Fig. 4) interact with a shock front that is moving rapidly forward through the simulation domain, and so do not gain sufficient velocity to outpace it. The ions that interact later (lower group in Fig. 4) meet a weakening shock front with a wider potential well, so that they are not reflected. In contrast to Fig. 2, the ions in Fig. 4 experience neither an x -energy gain on moving back to the upstream side of the potential well, nor a sustained period of y -energy gain as they subsequently co-move with the upstream edge of the well.

The present results suggest that the time-evolving shock dynamics, and in particular the timing of the interaction between ion and shock, govern the selection process determining which ions undergo pre-acceleration into a suprathermal population that may subsequently become cosmic rays.

IV. CONCLUSIONS

We have examined in detail the dynamics of suprathermal ions generated in PIC code simulations of quasi-perpendicular reforming shocks. Importantly, this energisation is not found in stationary shock solutions. We find that:

1. The shock structure reforms on a timescales of the order of the local ion cyclotron period. This is shown clearly if the electromagnetic fields are cast in the form of a potential, after removing small scale effects, to leave only terms relevant on ion spatio-temporal scales.
2. The time-dependence of the shock dominates the selection of which ions are accelerated to suprathermal energies. Ions that reach the shock when its ramp, and hence potential, are maximal, are reflected and subsequently gain energy by drifting in the time-dependent fields tangential to the shock front.
3. This selection is in contrast to a time-stationary shock, where the selection mechanism depends upon the initial ion velocity perpendicular to the magnetic field, those ions coming from the tails of the distribution being preferentially reflected, and so energised.
4. These factors lead to high energy ion creation occurring in bursts.

The present simulations are conducted in a $1x3v$ geometry at a low m_i/m_e . Whilst the work in Ref. [18] shows no major differences in higher spatial dimensions for PIC simulations, hybrid simulations in $2x3v$, for longer run times, show that the current that can now exist along the shock front can lead to current-driven instabilities [26]. These instabilities may act to change the shock structure in the y -direction, and so alter ion and electron dynamics across the shock front, affecting both ion and electron acceleration. Simulations with more realistic m_i/m_e ratios [11, 21] show alterations in the electron scale physics in the foot region. However, we have shown that the electron scale physics has little effect on ion spatio-temporal scales.

The plasmas simulated here are pure hydrogen, in that there are only two species, protons and electrons. Both species have a Maxwellian distribution with the same temperature. The addition of pickup ions to the simulation, for example in relation to the heliospheric termination shock, where hybrid simulation have already been carried out [27, 28], would allow the acceleration processes relevant to anomalous cosmic ray production to be examined. This will be the subject of future work.

The fundamental plasma physics processes underlying the ion acceleration from background to suprathermal energies (10 to 20 MeV), reported in the SNR shock simulations of Ref. [12], have been elucidated in the present paper. Specifically, we have explained the role of, and interplay between, the key elements anticipated at the end of the Appendix to Ref. [12]. We have shown that, while an electron fluid approximation captures some of the key physics, the shock reformation dynamics arising from our fully kinetic PIC treatment are central to the ion acceleration mechanism. This work provides a clear first principles explanation for the ion acceleration that is observed in our simulations, which appears to be a strong candidate injection mechanism for Galactic cosmic ray protons.

Acknowledgments

R. E. L. acknowledges a CASE Research Studentship from the UK Particle Physics and Astronomy Research Council in association with UK Atomic Energy Authority and a Warwick Postgraduate Research Fellowship from the University of Warwick. This work was also supported in part by the UK Engineering and Physical Sciences

Research Council. S. C. C. acknowledges the Radcliffe Foundation, Harvard.

-
- [1] K. Koyama, R. Petre, and E. V. Gotthelf, *Nature* **378**, 255 (1995).
 - [2] R. Enomoto, T. Tanimori, T. Naito, T. Yoshida, S. Yanagita, M. Mori, P. G. Edwards, A. Asahara, G. V. Bicknell, S. Gunji, et al., *Nature* **416**, 823 (2002).
 - [3] E. Fermi, *Phys. Rev.* **75**, 1169 (1949).
 - [4] A. R. Bell, *Mon. Not. R. Astron. Soc.* **182**, 147 (1978).
 - [5] J. R. Jokipii, *Astrophys. J.* **313**, 842 (1987).
 - [6] D. A. Tidman and N. A. Krall, *Shock waves in collisionless plasmas* (Wiley, New York, 1971), p. 11.
 - [7] K. B. Quest, *Phys. Rev. Lett.* **54**, 1872 (1985).
 - [8] K. B. Quest, *Adv. Space Res.* **6**, 33 (1986).
 - [9] D. Burgess, W. P. Wilkinson, and S. J. Schwartz, *J. Geophys. Res.* **94**, 8783 (1989).
 - [10] N. Sckopke, G. Paschmann, S. J. Bame, J. T. Gosling, and C. T. Russell, *J. Geophys. Res.* **88**, 6121 (1983).
 - [11] M. Scholer, I. Shinohara, and S. Matsukiyo, *J. Geophys. Res.* **108**, 1014 (2003).
 - [12] R. E. Lee, S. C. Chapman, and R. O. Dendy, *Astrophys. J.* **604**, 187 (2004).
 - [13] H. Schmitz, S. C. Chapman, and R. O. Dendy, *Astrophys. J.* **579**, 327 (2002).
 - [14] H. Schmitz, S. C. Chapman, and R. O. Dendy, *Astrophys. J.* **570**, 637 (2002).
 - [15] C. K. Birdsall and A. B. Langdon, *Plasma physics via computer simulation* (Institute of Physics publishing, London, 1991), p. 11.
 - [16] P. E. Devine, S. C. Chapman, and J. W. Eastwood, *J. Geophys. Res.* **100**, 17189 (1995).
 - [17] M. E. Dieckmann, K. G. McClements, S. C. Chapman, R. O. Dendy, and L. O'C. Drury, *Astron. Astrophys.* **356**, 377 (2000).
 - [18] B. Lembège and P. Savoini, *Phys. Fluids B* **4**, 3533 (1992).
 - [19] D. C. Ellison and S. P. Reynolds, *Astrophys. J.* **382**, 242 (1991).
 - [20] N. Shimada and M. Hoshino, *Astrophys. J.* **543**, L67 (2000).
 - [21] B. Lembège and P. Savoini, *J. Geophys. Res.* **107**, 1037 (2002).
 - [22] C. B. Laney, *Computational Gas Dynamics* (Cambridge University Press, Cambridge, 1998), p. 214.
 - [23] S. C. Chapman and W. M. Dunlop, *J. Geophys. Res.* **91**, 8051 (1986).
 - [24] S. C. Chapman and S. J. Schwartz, *J. Geophys. Res.* **92**, 11059 (1987).
 - [25] M. M. Leroy, *Phys. Fluids* **26**, 2742 (1983).
 - [26] D. Winske and K. B. Quest, *J. Geophys. Res.* **93**, 9681 (1988).
 - [27] A. S. Lipatov and G. P. Zank, *Phys. Rev. Lett.* **82**, 3609 (1999).
 - [28] E. L. Lever, K. B. Quest, and V. D. Shapiro, *Geophys. Res. Lett.* **28**, 1367 (2001).

FIG. 1: $\phi = \int E_x dx$ from PIC code (gray), and $\phi_i = \int E_{x,i} dx$ calculated from Eq. (9) (black) along the trajectory of a high energy ion. In calculating $E_{x,i}$ we compute the ion flow velocity from the mean velocity of all ions within $0.02\lambda_{ci} \simeq \lambda_{ce}/2 \simeq 10$ grid cells of the particle position.

FIG. 2: Trajectories for 4 ions that reach high energies. Panel 1 shows $\int q\mathbf{E} \cdot \mathbf{v} dt$ along each trajectory. Panel 2 the x -component of $\int q\mathbf{E} \cdot \mathbf{v} dt$, panel 3 the y -component. The z -component is not shown as it remain identically 0. Panel 4 displays $\phi = \int E_x dx$. Panel 5, y -position and panel 6, x -position plotted over the potential on ion scales, derived from Eq. (9), here the shock is propagating towards lower values of x as t increases. The vertical lines correspond to times of change during the black trajectory.

FIG. 3: Position x vs. y for a high energy ion. This ion follows the black trajectory in Fig. 2 and the timing points $a-f$ are indicated.

FIG. 4: Trajectories for four ions that remain at low energies when crossing the shock front. Panels and colors are as Fig. 2.

FIG. 5: Position x vs. y for two low energy ions. The black and gray trajectories from Fig. 4 are represented here, with the timing points A, B, A', B' indicated.

FIG. 6: Kinetic energy calculated from Eq. (14) using the PIC simulation \mathbf{E} (gray) and that on ion scales \mathbf{E}_i (black) from Eqs. (9) and (10), for the black ion in Figs. 2 and 3. The bulk ion velocity $v_{ix,y}$ in Eqs. (9) and (10) is calculated from the mean velocity of the ions within 10 grid cells $\simeq 0.02\lambda_{ci} \simeq \lambda_{ce}/2$ of the particle position.

FIG. 7: Phase space plots of v_x (left) and v_y (right) vs. x for groups of particles from differing regions of initial velocity space, at the instant $t = 4 \times 2\pi\omega_{ci}^{-1}$.

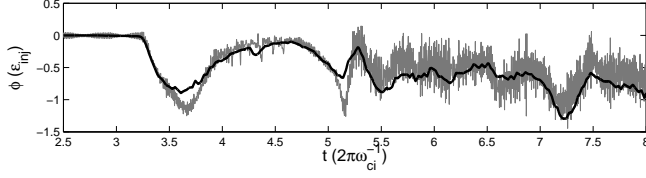


FIG. 1: $\phi = \int E_x dx$ from PIC code (gray), and $\phi_i = \int E_{x,i} dx$ calculated from Eq. (9) (black) along the trajectory of a high energy ion. In calculating $E_{x,i}$ we compute the ion flow velocity from the mean velocity of all ions within $0.02\lambda_{ci} \simeq \lambda_{ce}/2 \simeq 10$ grid cells of the particle position.

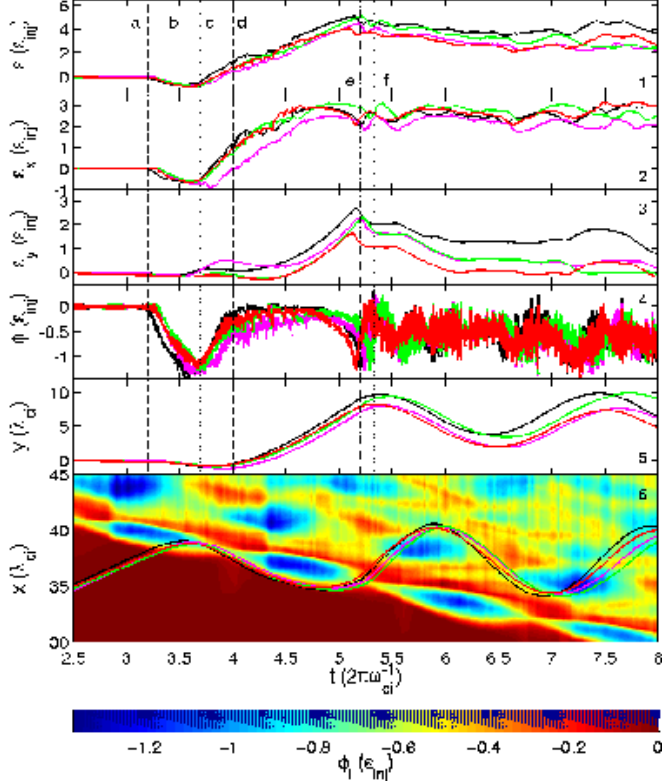


FIG. 2: Trajectories for 4 ions that reach high energies. Panel 1 shows $\int q\mathbf{E} \cdot \mathbf{v} dt$ along each trajectory. Panel 2 the x -component of $\int q\mathbf{E} \cdot \mathbf{v} dt$, panel 3 the y -component. The z -component is not shown as it remain identically 0. Panel 4 displays $\phi = \int E_x dx$. Panel 5, y -position and panel 6, x -position plotted over the potential on ion scales, derived from Eq. (9), here the shock is propagating towards lower values of x as t increases. The vertical lines correspond to times of change during the black trajectory.

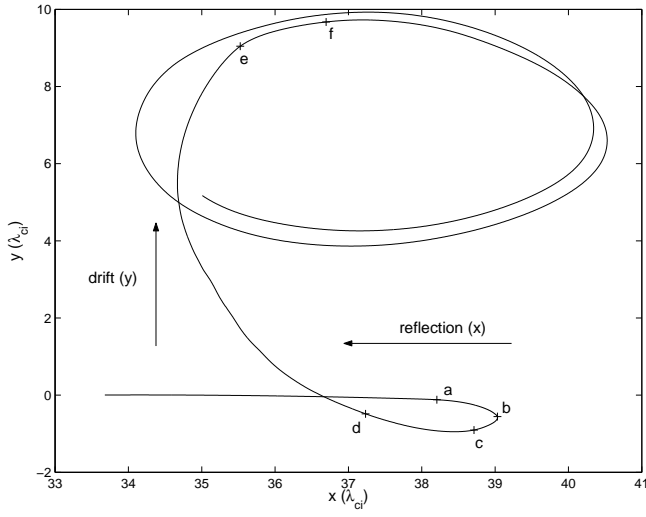


FIG. 3: Position x vs. y for a high energy ion. This ion follows the black trajectory in Fig. 2 and the timing points $a-f$ are indicated.

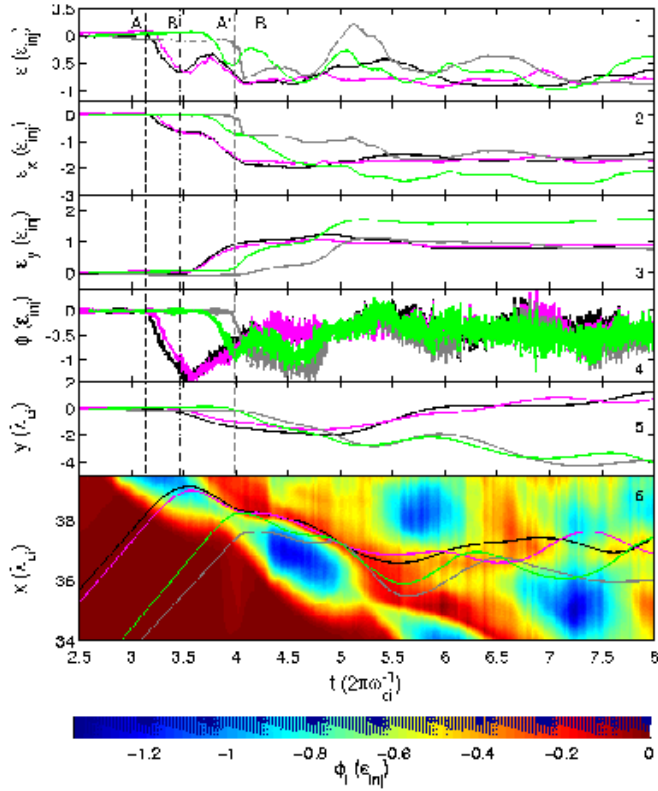


FIG. 4: Trajectories for four ions that remain at low energies when crossing the shock front. Panels and colors are as Fig. 2. Black vertical lines refer to the black trajectory, red lines to the red trajectory.

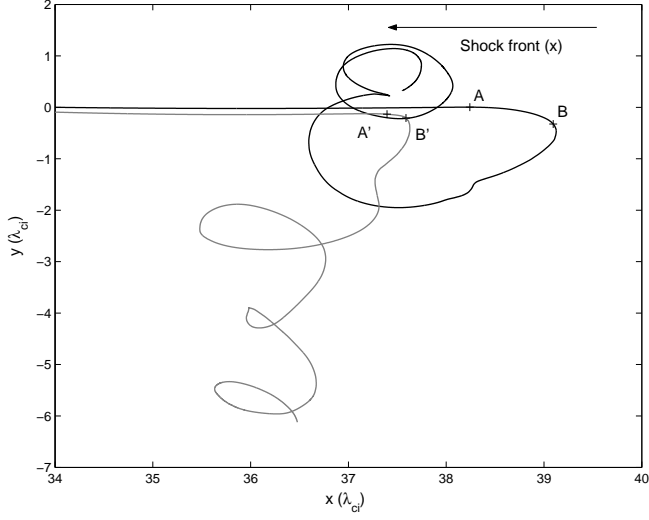


FIG. 5: Position x vs. y for two low energy ions. The black and gray trajectories from Fig. 4 are represented here, with the timing points A, B, A', B' indicated.

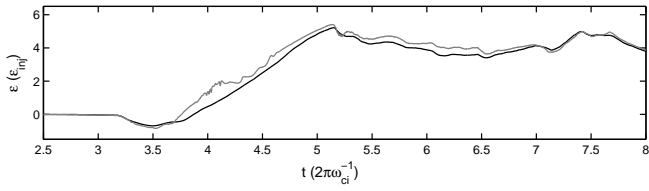


FIG. 6: Kinetic energy calculated from Eq. (14) using the PIC simulation \mathbf{E} (gray) and that on ion scales \mathbf{E}_i (black) from Eqs. (9) and (10), for the black ion in Figs. 2 and 3. The bulk ion velocity $v_{ix,y}$ in Eqs. (9) and (10) is calculated from the mean velocity of the ions within $10 \text{ grid cells} \simeq 0.02\lambda_{ci} \simeq \lambda_{ce}/2$ of the particle position.

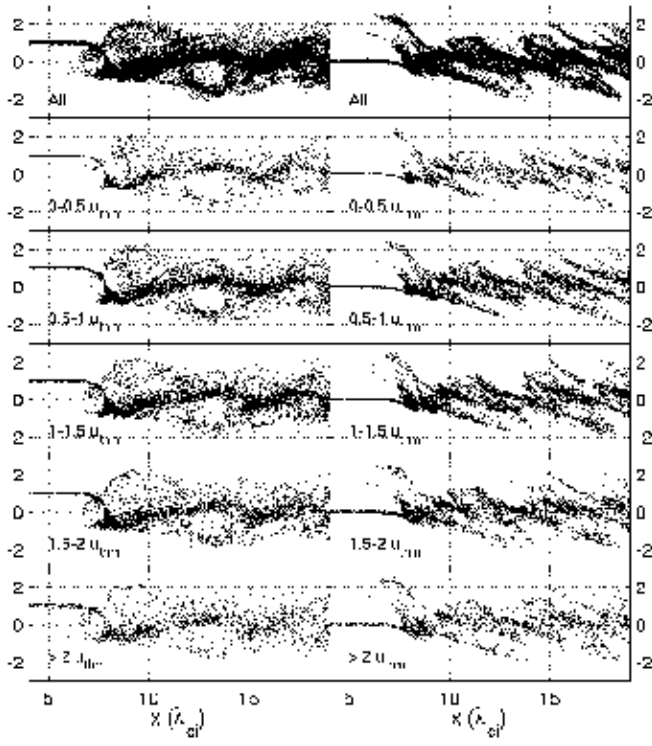


FIG. 7: Phase space plots of v_x (left) and v_y (right) vs. x for groups of particles from differing regions of initial velocity space, at the instant $t = 4 \times 2\pi\omega_{ci}^{-1}$.